Available online at www.sciencedirect.com

ScienceDirect

Russian Geology and Geophysics 48 (2007) 1–17

RUSSIAN GEOLOGY
AND GEOPHYSICS

www.izdatgeo.ru/index.php?action=journal&id=4

Moho depths and three-dimensional velocity structure of the crust and upper mantle beneath the Baikal region, from local tomography

A.V. Yakovlev, I.Yu. Kulakov, S.A. Tychkov

Institute of Geology and Mineralogy, Siberian Branch of the RAS, 3 prosp. Koptyuga, Novosibirsk, 630090, Russia

Received 11 September 2005, accepted 2 March 2006
Available online xx January 2007

Abstract

We studied the 3D velocity structure of the crust and uppermost mantle beneath the Baikal region using tomographic inversion of ~25,000 *P* and *S* arrivals from more than 1200 events recorded by 86 stations of three local seismological networks. Simultaneous iterative inversion with a new algorithm for source location yielded 3D images of *P* and *S* velocity anomalies in the crust and upper mantle, a 2D model of Moho depths, and corrections to source coordinates and origin times. The resolving power of the algorithm, its stability against variations in the starting model, and the reliability of the final results were checked in several tests. The 3D velocity structure shows a well-pronounced low-velocity zone in the crust and uppermost mantle beneath the southwestern flank of the Baikal rift which matches the area of Cenozoic volcanism and a high velocity zone beneath the Siberian craton. The Moho depth pattern fits the surface tectonic elements with thinner crust along Lake Baikal and under the Busiyngol and Tunka basins and thicker crust beneath the East Sayan and Transbaikalian mountains and under the Primorsky ridge on the southern craton border.

© 2007 Elsevier Ireland Ltd. All rights reserved

Keywords: Seismic tomography, earthquake location, Moho, Baikal Rift

Introduction

Tectonics of the study region. The Baikal region is located at the boundary between the southeastern margin of the Siberian craton and the Amur-Mongolia plate which belongs to the Alpine-Himalayan orogen. The Cenozoic evolution of the region has been controlled by the joint effect of compression from the India-Eurasia collision responsible for active mountain building (East Sayan mountains) and extension that produced the Baikal rift.

The Baikal rift, the main tectonic unit of the region, extends along the southern craton edge. Its NEN central segment delineates Lake Baikal, the eastern rift flank strikes to the northeast, and the western flank kinks at the Tunka rift basin to turn south (Busiyngol, Darhat, and Hovsgol basins) (Khain, 2001). In the southwest, in Mongolia, the rift system is truncated by the W-E Bulnayn strike-slip fault (Fig. 1) (Zorin et al., 2003).

The rift basins are separated by necks and make up a complex elongate branching system. Most of large basins (South Baikal, Barguzin, Muya, Chara) align with the rift axis but some (North Baikal and Upper Angara) step off towards the northwestern flank of the Sayan-Baikal uplift (Logatchev and Zorin, 1987).

The position of the Baikal rift was interpreted as a result of large-scale lithospheric heterogeneities (Logatchev, 1993). Yet, rifting in the northeastern flank of the system shows independence from the prerift basement framework as the rift elements within the Muya microcontinent crosscut the basement structures, together with the Sayan-Baikal fold belt, and advance further into the eastern Aldan shield. Logatchev (1993) attributed this partial independence of the rift to local mismatch between the general orientation of the asthenospheric upwarp, the major agent in the Baikal Cenozoic rifting, and the direction of some fold belt structures.

Late Cenozoic rifting was almost continuously accompanied by volcanism which was, however, minor in volume and distributed in a peculiar way relative to the rift structures. Lavas of basaltic and similar major-element compositions occur in three independent groups of volcanic fields in the southwestern (East Sayan and Khamar-Daban mountains and North Mongolia) and northeastern (Vitim plateau and Udokan Ridge, off the study region) rift flanks (Fig. 1). Volcanic

---

* Corresponding author.
E-mail address:

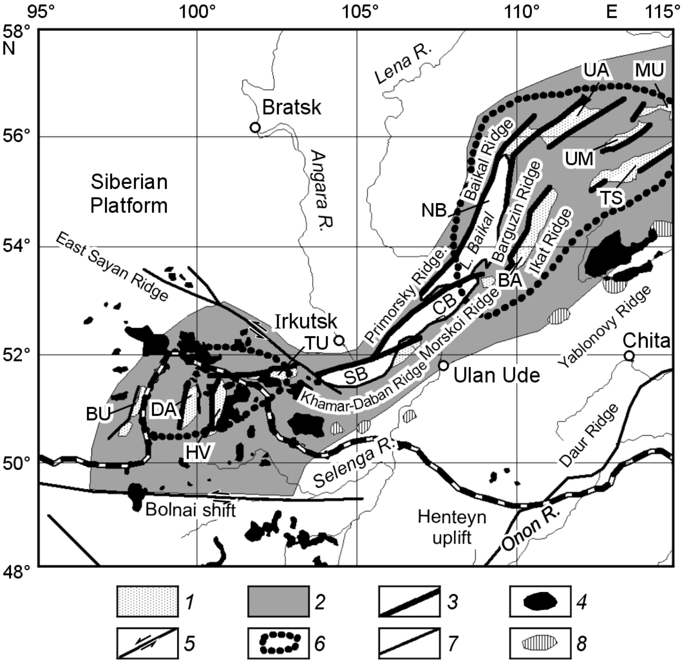

Fig. 1. Quaternary tectonics and volcanism in the Baikal region, after (Zorin et al., 2003). *1* — rift basins (listed in northeastern direction), abbreviated as: BU — Busiyngol, DA — Darhat, HB — Hovsgol (lake), TU — Tunka, SB — South Baikal, CB — Central Baikal, NB — North Baikal, UA — Upper Angara, BA — Barguzin, TS — Tsypa, UM — Upper Muya, MU — Muya; *2* — Baikal rift system; *3* — vertical faults; *4* — Oligocene-Quaternary volcanics; *5* — strike-slip faults; *6* — contour of Sayan-Baikal uplift (mountains occasionally reaching 2000 m asl); *7* — Cenozoic faults of uncertain geometry; *8* — Late Cretaceous-Paleogene volcanics (out of scale).

activity was the most intense in the Miocene and decayed in Pliocene and Quaternary time (Logatchev and Zorin, 1987).

Geophysical data. The Baikal rift system has been largely covered by geophysical surveys of the crust and upper mantle but the results are often controversial. We cite three models of the Moho geometry (Fig. 2). Suvorov et al. (2002) inferred Moho depths from refraction and wide-angle reflection data (Fig. 2, *a*) and Logatchev and Zorin (1987) used correlation between the Moho depth and surface topography (Fig. 2, *b*) and referred to crustal thickness data from (Puzyrev, 1981). The third model (Fig. 2, *c*) is part of the 2°×2° CRUST2.0 global model (Bassin et al., 2000) and results from compilation of various data, including the Moho map for the Baikal region from (Belousov et al., 1991).

The three models agree in the most general points and disagree in many details, possibly because the Moho shows up in different ways in seismic and gravity fields but more likely because of the limitations of the methods.

The Moho depth ranges in the three models are between 30 and 40 km beneath the rift basins, 45–50 km under the bordering mountains, and 40–42 km beneath the Siberian craton (Logatchev and Zorin, 1987).

DSS surveys along many regional profiles (Puzyrev, 1981, 1993; Song Youngsheng et al., 1996), together with evidence from local earthquakes (Krylov et al., 1974; Puzyrev, 1981), indicate that the crust beneath Lake Baikal is underlain by an asthenospheric upwarp with *P*-wave velocities lower than on the rift periphery (7.7–7.8 km/s against 8.1–8.2 km/s) (Khain, 2001; Logatchev and Zorin, 1987; Puzyrev, 1981, 1993; Song Youngsheng et al., 1996). Low mantle velocities beneath the rift and its surroundings are indicated by *P*-wave travel time data from remote earthquakes and blasts (Rogozhina and Kozhevnikov, 1979) and by regional (Koulakov et al., 2002) and global (Bijwaard et al., 1998) seismic tomography. More evidence comes from analysis of receiver functions (Zorin et al., 2002) from rift-orthogonal profiles.

Many papers address gravity modeling for the structure of the Baikal region. Among others, Burov et al. (1994) modeled the gravity field along a profile in the northern Baikal rift system; Tiberi et al. (2003) obtained density and velocity patterns in the crust and upper mantle using joint inversion of seismic and gravity data.

Much work has been done to study seismicity in the Baikal rift system, an active seismic area, where about 7000 $M > 2.7$ events were recorded in the Central and South Baikal basins

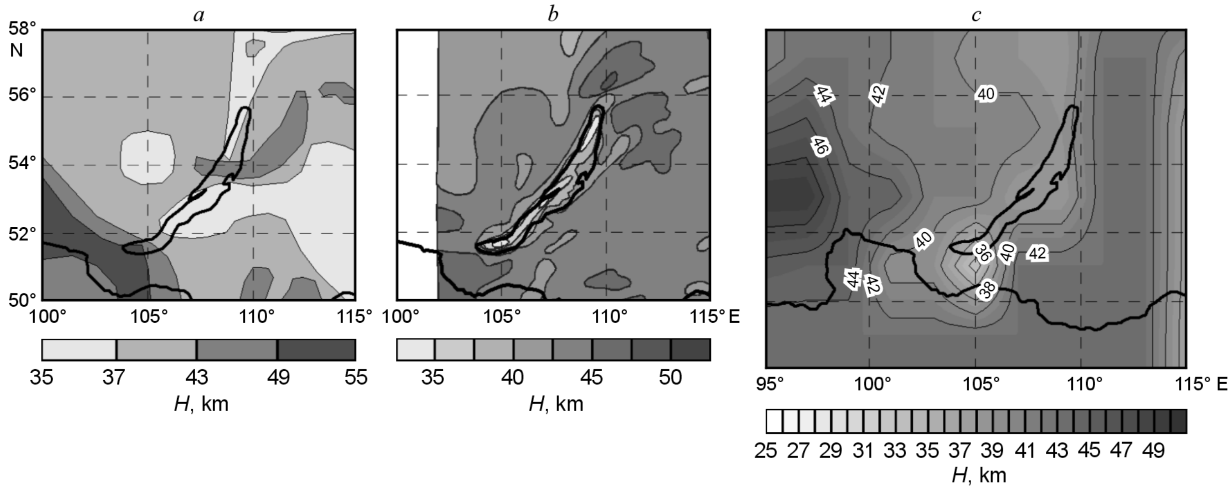

Fig. 2. Crust thickness models: after (Suvorov et al., 2002) (*a*), after (Logatchev and Zorin, 1987) (*b*), and 2°×2° CRUST2.0 model (Bassin et al., 2000) (*c*).

between January 1950 and January 1999 (Radziminovich et al., 2003). Deverchere et al. (2001) located earthquake hypocenters to investigate the regional rheology. Radziminovitch et al. (2005) described surface rupture produced by the M = 6 earthquake of 1999 in the southern Baikal rift and constrained the position of the fault plane from the aftershock sequence.

Calais et al. (2003) estimated the velocities and directions of motion of major tectonic elements in the Baikal region and Mongolia from GPS measurements of active deformation. They infer extension at 2.5–3 mm/yr in the central rift segment and mainly left-lateral strike-slip faulting in its southwestern flank.

Geothermal data indicate higher heat flux in the rift relative to the adjacent regions: 75–120 mW/m^2 against 38–42 mW/m^2 in the Siberian craton and 40–60 mW/m^2 in its folded surroundings (Fig. 3) (Dorofeeva and Sintsov, 1990; Duchkov and Sokolova, 1974; Duchkov et al., 1987; Khain, 2001; Lysak, 1984, 1988).

Seismic tomography has become recently a common tool to image the lithosphere of the Baikal region. The 3D velocity structure of the crust and upper mantle was derived from global (Bijwaard, 1998), regional (Kulakov, 1999; Koulakov and Tychkov, 2002; Mordvinova et al., 2000), and local (Kulakov, 1999; Petit et al., 1998) tomography studies.

Origin of the Baikal rift: geodynamic models. The Baikal region with its complex structure and tectonic history attracts much attention of Earth scientists. The rift origin has been explained in terms of two alternative hypotheses and their various combinations. One hypothesis attributes rifting to extension caused by the activity of a large plume (Logatchev and Zorin, 1987; Logatchev, 1993; Zorin and Turutanov, 2005) and stems from the evidence of active Cenozoic volcanism (Zorin et al., 2003), high heat flux (Dorofeeva and Sintsov, 1990; Duchkov et al., 1987; Duchkov and Sokolova, 1974; Lysak, 1984, 1988) and low seismic velocities beneath the rift (Puzyrev, 1981, 1993; Song Youngsheng et al., 1996). The alternative hypothesis invokes far-field effects of the India-Eurasia collision and the Pacific subduction (Nicolas et al., 1994; Peltzer and Tapponnier, 1988; Zonenshain and Savostin, 1980) and is supported by low intensity of thermal effects in the Baikal rift system insufficient to account for active rifting and the lack of volcanism in the most strongly extended Baikal basin.

The models that combine the two approaches differ in estimating the contribution of mantle processes to the rift origin. Some models explain lithospheric extension beneath Lake Baikal by heating from a mantle plume (Kulakov, 1999; Petit et al., 1998) which produces a zone of weakness accommodating the far-field collisional stresses. Others consider plate interaction as a major agent (Achauer, 2002; Chemenda, 2002; Lesne, 2000) and presume that extension along the boundary of Siberia is controlled by uneven lithospheric strength. According to this interpretation, the presence of low-velocity mantle beneath the Baikal rift is the effect rather than the cause of extension, as mantle becomes drawn into the extended zone.

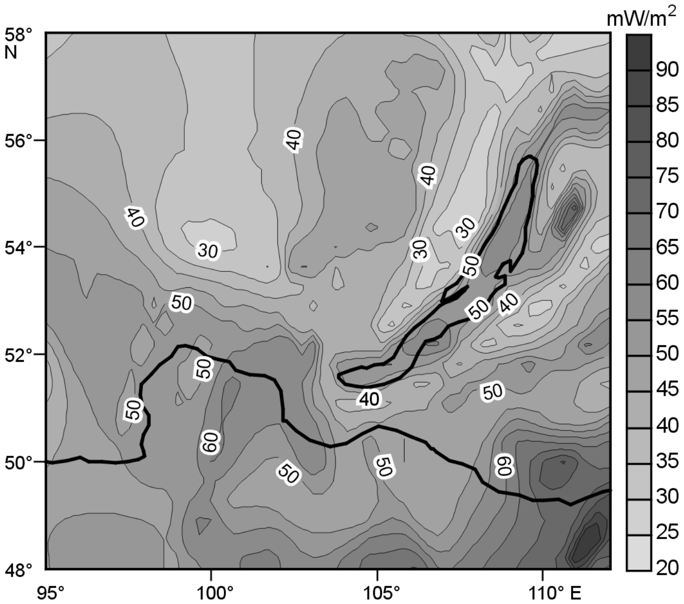

Fig. 3. Heat flow map of study region (data for 1974–1990), after (Dorofeeva and Sintsov, 1990; Duchkov et al., 1987; Duchkov and Sokolova, 1974; Lysak, 1984, 1988).

The controversy about the suggested origin mechanisms of the Baikal rift is to a great extent due to the lack of knowledge on its deep structure (see, for instance, the three different Moho maps in Fig. 2). Though largely documented, the crust and upper mantle structure beneath the Baikal rift has so far eluded a comprehensive interpretation. A better understanding can be gained with independent methods.

We report the 3D velocity structure of the crust and upper mantle beneath the Baikal region obtained by tomographic inversion of P and S arrivals from local earthquakes using a large collection of initial data on the 3D deep structure of the rift and its surroundings. We hope our study helps getting a deeper insight into the origin mechanism of the Baikal rift.

Algorithm

Reference model and travel times. The inversion is performed using a 1D spherical reference velocity model. At the initial stage, we compute a table of travel times of P and S body waves in the reference model for different source depths which allows a prompt estimation of the parameters of basic rays between a source at some depth and a station at the sea level some distance away from the source. Yet, estimates with the use of the 1D reference model, assuming a flat Moho, can bear large error in regions where Moho depths and surface topography show considerable variations. For instance, crust thickness difference in the Baikal region reaches 10 km which causes 0.72 s changes to travel times. Neglect of this fact is fraught with large errors in source locations and in travel time residuals. Therefore, it appears reasonable to include any (even very preliminary) information on the Moho depth into the reference model. The Moho depth correction is applied as a nonspherical term added to travel times. For sources below the Moho, it is found as

$$dt^{\text{moho}} = dh\,[\sqrt{\sigma_1^2 - p^2} - \sqrt{\sigma_2^2 - p^2}], \tag{1}$$

where σ_1 and σ_2 are the slowness values immediately above and below the Moho, respectively; p is the ray parameter (the horizontal component of the slowness vector), dh is the deviation of Moho depth at the entry point from its average in the reference model.

The Moho depth correction for head waves (P_n and S_n rays refracted at the Moho) is given by

$$dt^{\text{moho}} = (dh_1 + dh_2)\sqrt{\sigma_1^2 - \sigma_2^2}, \tag{2}$$

where dh_1 and dh_2 are crust thickness variations beneath the receiver and the source, respectively.

The terrain correction for surface topography is likewise computed as an additional term:

$$dt^{\text{moho}} = dh\sqrt{\sigma^2 - p^2}, \tag{3}$$

where dh is the height of the station above the sea level and σ is the slowness in the upper layer.

Source location algorithm. The suggested source location algorithm includes several successive steps. The first step implies absolute location in a 1D reference model corrected for Moho depth variations and surface topography. The following step consists in relative relocation of sources using the double difference method. The final relocation is achieved by simultaneous inversion for velocities and Moho depths.

The absolute source location is the key point in the inversion procedure. If it is wrong, further corrections will hardly provide authentic results.

Mislocation is primarily due to outliers in the initial data set. We estimate that residuals in 5–10% of ISC data cannot be explained by a reasonable velocity model. Outliers can be caused by errors in phase picking, operator's mistakes, instrumental problems, and other objective and subjective factors. One or several outliers can cause a considerable source mislocation, bias origin times and change other residuals further used in velocity modeling. Large outliers are picked and rejected at the preprocessing stage but small ones are quite difficult to pick and cause the greatest problem. We suggest to reject outliers at the step of absolute source location using a special analysis of residuals (see below).

Wrong phase identification is another cause of errors. For instance, a travel time between those of P_n and P_g phases in the reference model can be assigned to this or that phase. The resulting residual in the case of misidentification can have a wrong sign which causes errors in velocities and source location.

The source location algorithm should take these problems into account. A key part in the algorithm belongs to the goal function corresponding to the probability of source location in the 4D space (coordinates and origin time). We suggest to represent the goal function as a combination of three terms as

$$G = \sum_{i=1}^{N} A\,(\Delta t_i) B\,(d_i)/C_{PS}, \tag{4}$$

where:

$$A\,(\Delta t_i) = \begin{cases} 1, & |\Delta t_i|/C_{PS} < \tau_1 \\ (\Delta t_i - \tau_2)/(\tau_1 - \tau_2), \text{ if } & \tau_1 < |\Delta t_i|/C_{PS} < \tau_2\,, \\ 0, & |\Delta t_i|/C_{PS} > \tau_2 \end{cases} \tag{5}$$

$$B\,(d_i) = \begin{cases} 1/d_{\min}, & \text{if } d_i < d_{\min} \\ 1/d_i, & \phantom{\text{if }} d_i > d_{\min} \end{cases}, \tag{6}$$

$$C_{PS} = \begin{cases} 1, & \text{if } P \text{ wave} \\ 1.7, & \phantom{\text{if }} S \text{ wave} \end{cases}. \tag{7}$$

The term A allows for the value of residuals, where τ_1 and τ_2 are their user specified limits. Residuals above τ_2 are taken for outliers and are rejected. Sources are located mainly from residuals below τ_1. Residuals between τ_1 and τ_2 can be interpreted as a velocity anomaly but it has a smaller contribution to the goal function.

The term B is distance-dependent, and $d_{\min}$ is the size of the near-field zone within which the rays have equal weights.

The term C discriminates between phases. Residuals of P rays have a greater weight being less dependent on velocity variations than S rays, but S residuals are allowed to be greater than P residuals.

Travel time residuals are computed as

$$\Delta t_i^P = t_{\text{obs}}^P - t_{\text{ref}}^P - \Delta t_0 \text{ for } P \text{ wave}, \tag{8}$$

$$\Delta t_i^S = (t_{\text{obs}}^S - t_{\text{ref}}^S) - (t_{\text{obs}}^P - t_{\text{ref}}^P) \text{ for } S \text{ wave}. \tag{9}$$

This equation choice for S waves improves correlation between P and S residuals. However, a lower weight of the latter reduces the contribution from the minimization of difference residuals.

The origin time correction Δt_0 is given by

$$\sum_{i=1}^{N_p} B\,(d_i)\,(t_{\text{obs}}^P - t_{\text{ref}}^P - \Delta t_0) = 0, \tag{10}$$

where t_{obs}^P is the recorded travel time and Δt_{ref}^P is the travel time in the reference model.

Each specific observation should satisfy the condition

$$|t_{\text{obs}}^P - t_{\text{ref}}^P - \Delta t_0| < \tau_2, \tag{11}$$

and the others are considered as outliers and are neglected. If several phases are possible within a given epicentral distance (e.g., P_g and P_n), we select the phase that has the least residual and, hence, provides the maximum value of the goal function. Figure 4 shows an example goal function for a real event computed at two different depths. The most probable source location is selected according to the maximum value of the goal function.

There are different approaches to solve the problem for the goal function absolute extreme. Gradient methods can provide

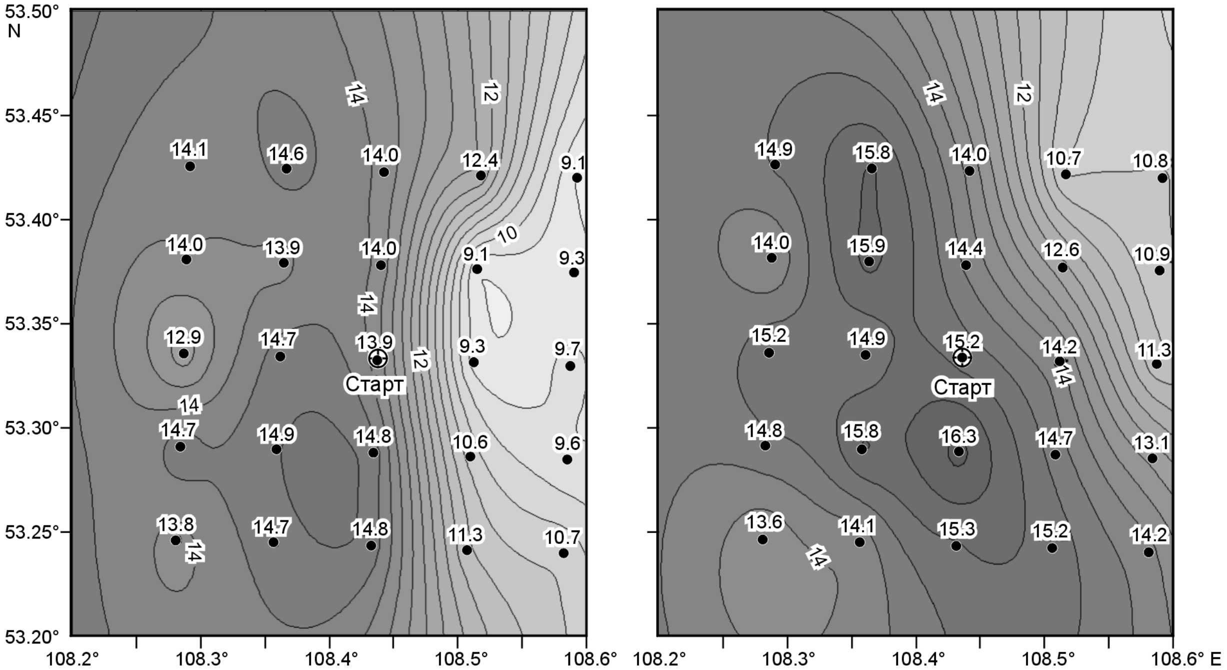

Fig. 4. Example of computed goal function for a real event at different depths.

fast convergence but there is a risk to take a local maximum for the absolute extreme. We use a longer but a more stable way of computing in grid nodes (Fig. 4). The goal function is first estimated on a sparse grid for three or four depths. Then, we move up and down from the level of the goal function maximum to fit the depth corresponding to the extreme (see an example depth dependence of the goal function in Fig. 5). Then we use a finer 3D grid to update the extreme position which indicates the most probable source location in the given model.

Double-difference source relocation. The relative position of sources is adjusted using the double difference method (Waldhauser and Ellsworth, 2000). The basic idea of the method stems from the assumption of the similarity of phase residuals from two nearby sources recorded at the same station. The algorithm computes location and origin time corrections to minimize all possible double differences. The linear equation for all possible combinations of source pairs (e.g., k and m) which are spaced at a distance no longer than $dS^{\max}$ and correspond to the same observation I (one station one recorded phase P or S) is

$$(P_x)_{ik}\,dx_k + (P_y)_{ik}\,dy_k + (P_z)_{ik}\,dz_k + dt_k^0 - (P_x)_{im}\,dx_m - (P_y)_{im}\,dy_m - (P_z)_{im}\,dz_m - dt_m^0 = dt_{ik}^{\text{obs}} - dt_{im}^{\text{obs}}. \qquad (12)$$

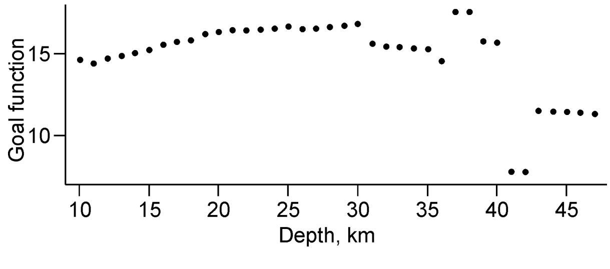

Fig. 5. Example of depth dependence of goal function.

As a result, we obtain a system of linear equations with the same number of unknowns equal to the four-fold number of sources. Each line of the system has eight nonzero elements. A system for 1200 sources spaced at $dS^{\max} = 20$ km includes about 500 000 equations and is solved by LSQR iteration (Paige and Saunders, 1982; van der Sluis, van der Vorst, 1987). After the system has been solved, the sources are relocated and the updated locations are used to obtain a new double difference matrix. In our experiments four or five iterations were required.

Iterative tomographic inversion. The velocity and Moho depth fields are parameterized using the node parameterization method (Petit et al., 1998; Radziminovich et al., 2003). The velocity grid nodes are distributed within the imaged volume according to the input data density. In the 3D velocity model for the crust, the nodes are distributed at several levels and the ray density function is computed for each level. The nodes at each level align with several parallel straight lines so that their spacing were inversely proportional to the ray density. The minimum spacing is fixed to avoid too high concentration of the nodes.

The Moho depth nodes are distributed in a similar way according to the density of entry and exit points of P_n and S_n rays at the Moho.

Matrix construction and inversion. The matrix used for simultaneous Moho depth and velocity inversion has its columns corresponding to 3D models of P and S velocities in the crust and upper mantle (M^{V_P}, M^{V_S}); 3D Moho depth variations (M^{dh}); source location corrections (four corrections for each source); and P and S station corrections.

The matrix elements M^{V_P} and M^{V_S} responsible for the crust

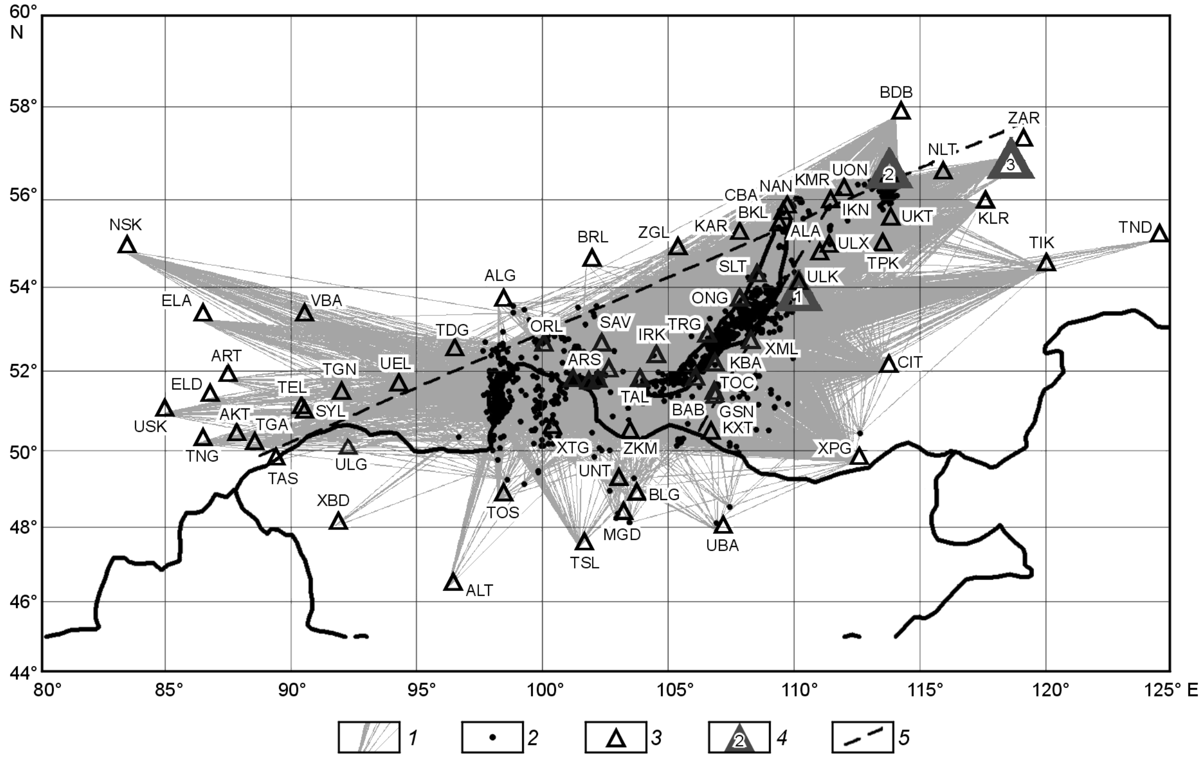

Fig. 6. Locations of sources and stations used in this study. *1* — rays; *2* — sources; *3* — stations; *4* — groups of stations: 1 — Barguzin group (BDN, BRG, JRV, NST, SVO), 2 — Upper Angara group (ANG, OZN, TNL, SMS, KVT, ORN, MKA, VRA, TRK), 3 — Chara group (CAR, EMG, LRB, UDK, NMG); *5* — campaign seismic profiles.

and upper mantle *P* and *S* velocity fields are computed using the rays traced after the double difference adjustment has been applied. Eight nodes of the parameterization grid are selected for each ray point so that they made a parallelogram containing the given point. The velocities inside the parallelogram are interpolated bilinearly. The matrix elements are computed as

$$M_{ij}^{V_P\,(S)} = -\frac{1}{\Delta V_j^{P\,(S)}} \int\limits_{\gamma_i} \frac{\Delta U_j\,(l)}{V_0^2(l)}\, dl, \qquad (13)$$

Table 1
Reference velocity model

Depth, km	V_P	V_S
	km/s	
–5	5.10	2.91
0	5.80	3.31
8	6.00	3.42
10	6.20	3.53
15	6.40	3.65
25	6.80	3.88
40	6.85	3.90
43	7.80	4.45
77.5	8.04	4.5
120	8.0	4.5

where *I* is the ray number (matrix line); *j* is the parameter number (matrix column); γ_i is the ray path; $\Delta V_j^{P\,(S)}$ is the unit velocity variation in the *j*-th node; $\Delta U_j(l)$ is the velocity variation at the current point caused by velocity variation in the node; $V_0(l)$ is the reference velocity at the current point.

The elements M_{ij}^{dh} which allow for Moho depth variations are found as

$$M_{ij}^{dh} = dh_{ij}\,[\sqrt{\sigma_1^2 - p^2} - \sqrt{\sigma_2^2 - p^2}], \qquad (14)$$

if the source is below the Moho and as

$$M_{ij}^{dh} = (dh_{ij}^1 + dh_{ij}^2)\,\sqrt{\sigma_1^2 - \sigma_2^2} \qquad (15)$$

for P_n and S_n rays.

There dh_{ij} is the Moho depth variation at one or two entry/exit points caused by a unit depth variation in the *j*-th node.

The elements responsible for the source correction include four terms. The first three elements of the space distribution are equal to the slowness vector components, and the fourth element corresponding to the origin time correction is unity. The elements of the station corrections are likewise unity.

The additional matrix block allows smoothness regularization of the obtained 2D and 3D fields. The block is constructed using all possible combinations of neighbor node pairs. Each block line (equation) includes two nonzero elements (+/–1) corresponding to one pair. The data vector in the block is zero.

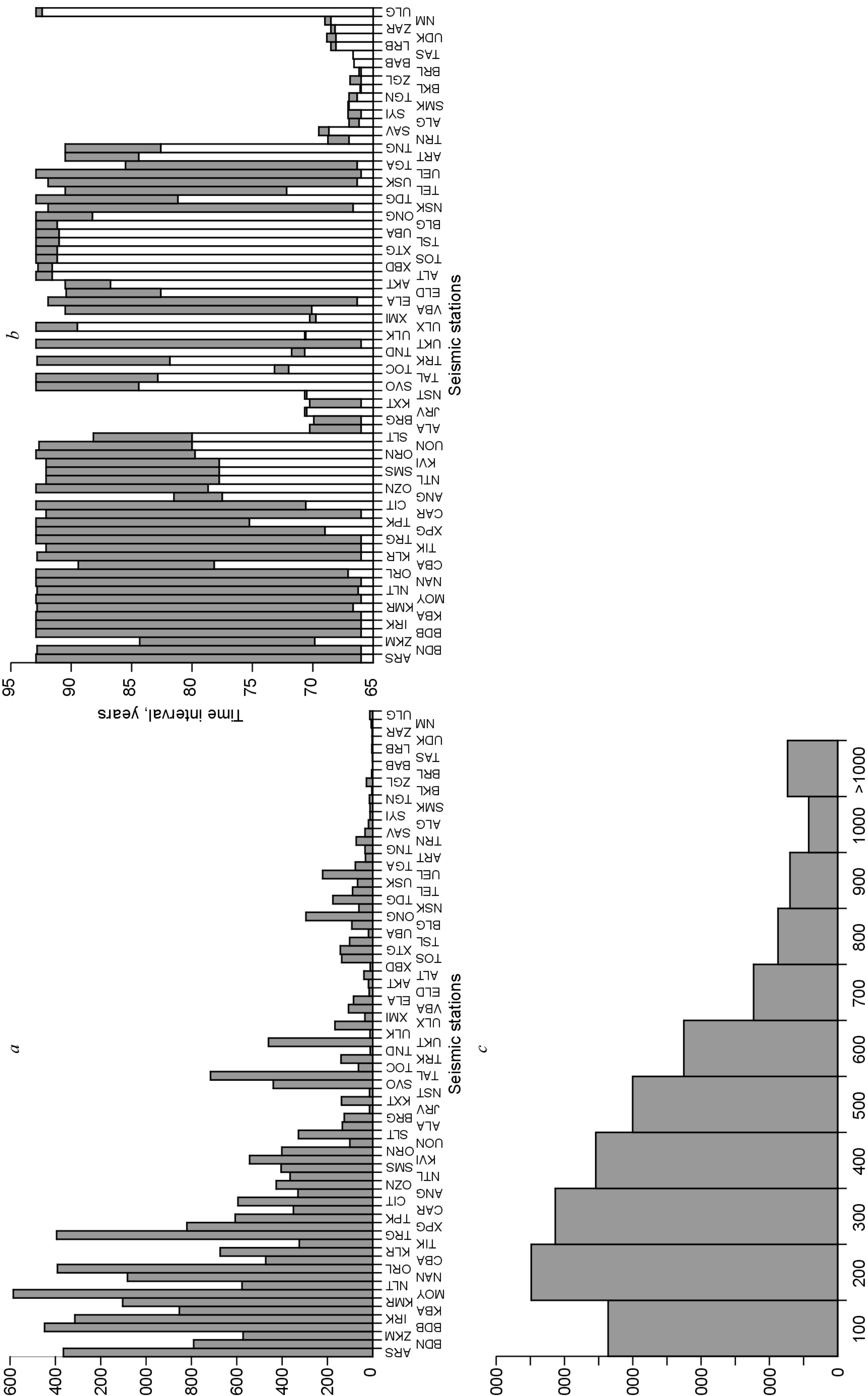

Fig. 7. Contribution of each station to the data set (*a*), time (year) of observations (*b*), epicentral distance histogram (*c*).

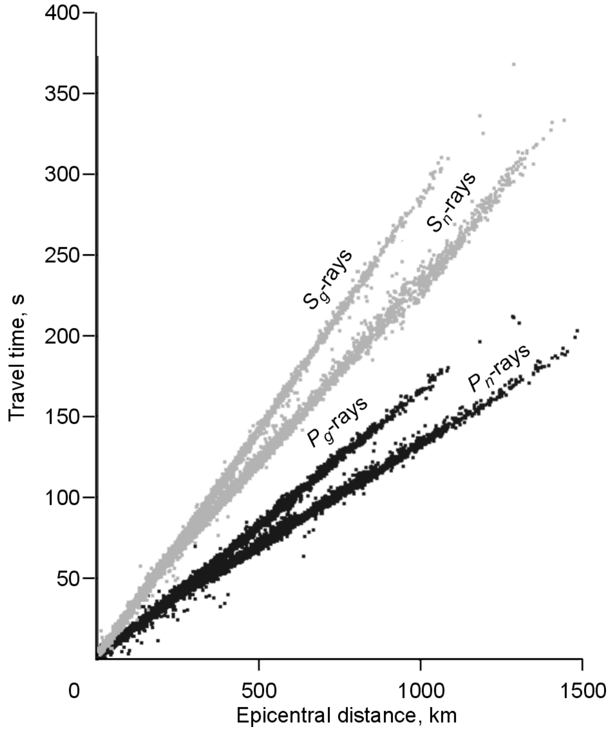

Fig. 8. Epicentral distance dependence of *P* and *S* travel times. *P* travel times are in black and *S* travel times are in gray.

Thus, the block minimizes the difference of the obtained parameters for the neighbor nodes.

As a result, we have eleven free weight coefficients to be determined: W_1 and W_2 allow for 3D anomalies of *P* and *S* velocities in the crust and upper mantle; W_3 is responsible for Moho depth variations; W_4 and W_5 correspond to *P* and *S* station corrections; W_6, W_7, and W_8 regulate vertical and horizontal source shifts and allow origin time correction; W_9, W_{10} and W_{11} provide smoothness control of the respective 2D and 3D fields. The greater the latter three coefficients, the smoother the solution. Finding the matrix coefficients is a hard problem. Their optimum parameters depend on different factors (quality and amount of data, expected values of the sought parameters, average number of records for each source, etc.) and are estimated experimentally, without any rigorous procedure, according to their expected values and synthetic tests. For instance, the weight coefficients can be found using the chequerboard test by selecting them in a way to achieve the best fit of the intensity and geometry of computed anomalies to the given values (see below). The resulting system is solved by the LSQR method (Paige, Saunders, 1982; van der Sluis, van der Vorst, 1987).

After the inversion, all rays from the relocated sources are retraced. Travel times are computed taking into account the parameters obtained at the previous step. As a result, residuals are updated, a new matrix is obtained, and inversion repeats. The iterative process continues as long as the contribution of some following step becomes vanishing (every following iteration reduces the scatter of residuals for less than 3%). We achieved convergence after four iterations.

Initial data for tomographic inversion

We used arrivals of crustal phases (P_g, S_g and P_n, S_n) recorded at 77 stations of the regional seismological network (Fig. 6) including the Altai-Sayan, Baikal, and Mongolia local data, and data from two campaign profiles. Note that 80% of observations come from 37 stations. Inversion was applied to ~14,000 and ~11,000 *S* rays from over 1200 events that occurred in the Baikal region between 1966 and 1990 with epicentral distances under 10–12° (Fig. 6). The panels *a*, *b*, and *c* of Fig. 7 show, respectively, the contribution of each station to the data set, the time (year) of observation, and the epicentral distance histogram.

The reference model (Table 1) was obtained using regional DSS results (Puzyrev, 1981; Song Youngsheng et al., 1996). We rejected a number of crustal *P* and *S* rays with long epicentral distances which apparently traveled along some intricate paths of internal interfaces and do not fit a 1D reference model (Fig. 8).

Figure 9 shows the patterns of *P* and *S* residuals before and after the absolute source location. The ray density at several levels (Fig. 10) demonstrates the “illumination” of the imaged volume. We used two starting models of crust thickness for the Baikal region. One assumes a flat Moho at 40 km and the other (Fig. 2, *c*), with a 2°×2° resolution, refers to integrate DSS and gravity data (Bassin et al., 2000).

Results

Synthetic tests. The obtained velocity and Moho depth models were checked by several synthetic tests.

The *chequerboard test* checks the ability of the algorithm to reconstruct staggered synthetic anomalies (Fig. 11). Travel times were computed by tracing actual rays through positive and negative anomalies with the amplitude ±5% alternating in

Table 2
Correlation of inversion results for initial locations of anomalies, chequerboard test

Model	Depth, km					
	5	20	40	43	60	Moho
P	0.400	0.336	0.495	0.461	0.503	0.492
S	0.371	0.403	0.432	0.375	0.386	

Table 3
Correlation of inversion results for two independent data sets (odd and even sources)

Model	Depth, km					
	5	20	40	43	60	Moho
P	0.457	0.472	0.646	0.507	0.047	0.389
S	0.389	0.497	0.598	0.665	0.247	

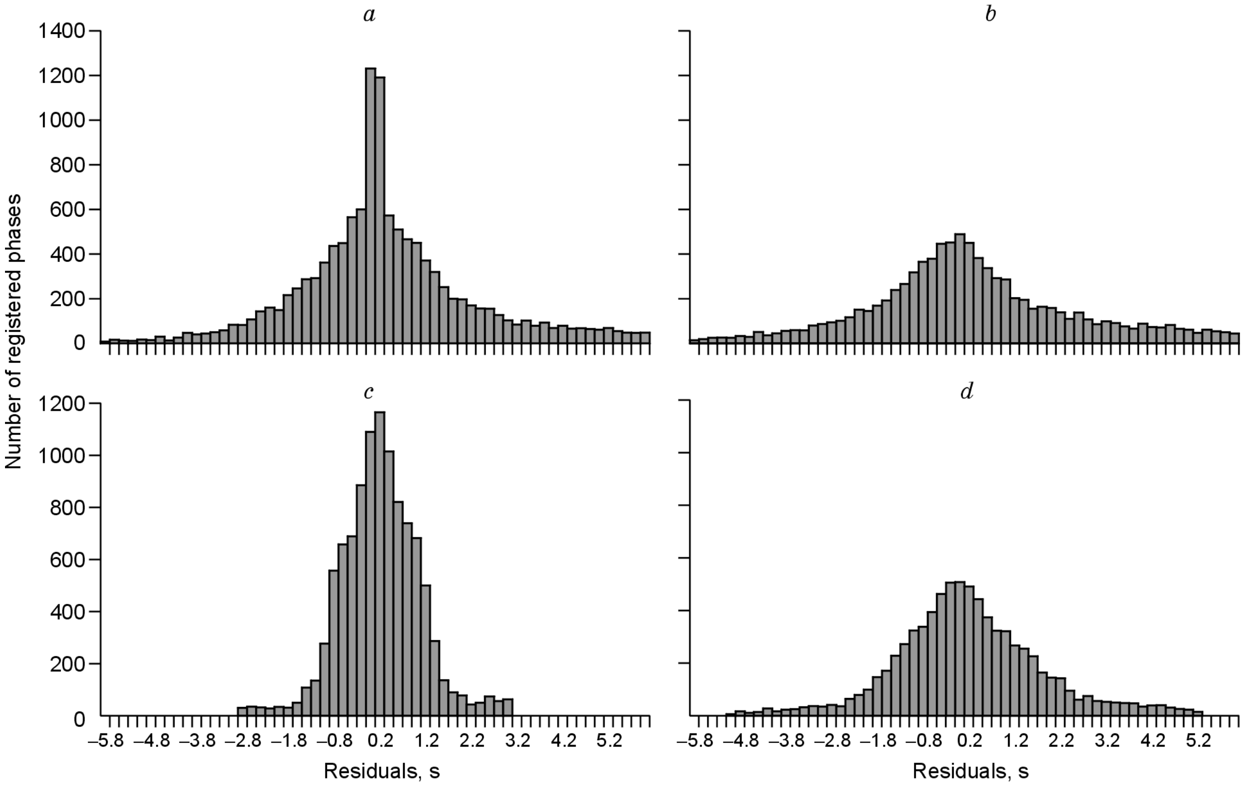

Fig. 9. Histograms of P and S travel time residuals before (*a*, *b*) and after (*c*, *d*) location. *a*, *c* are P residuals and *b*, *d* are S residuals.

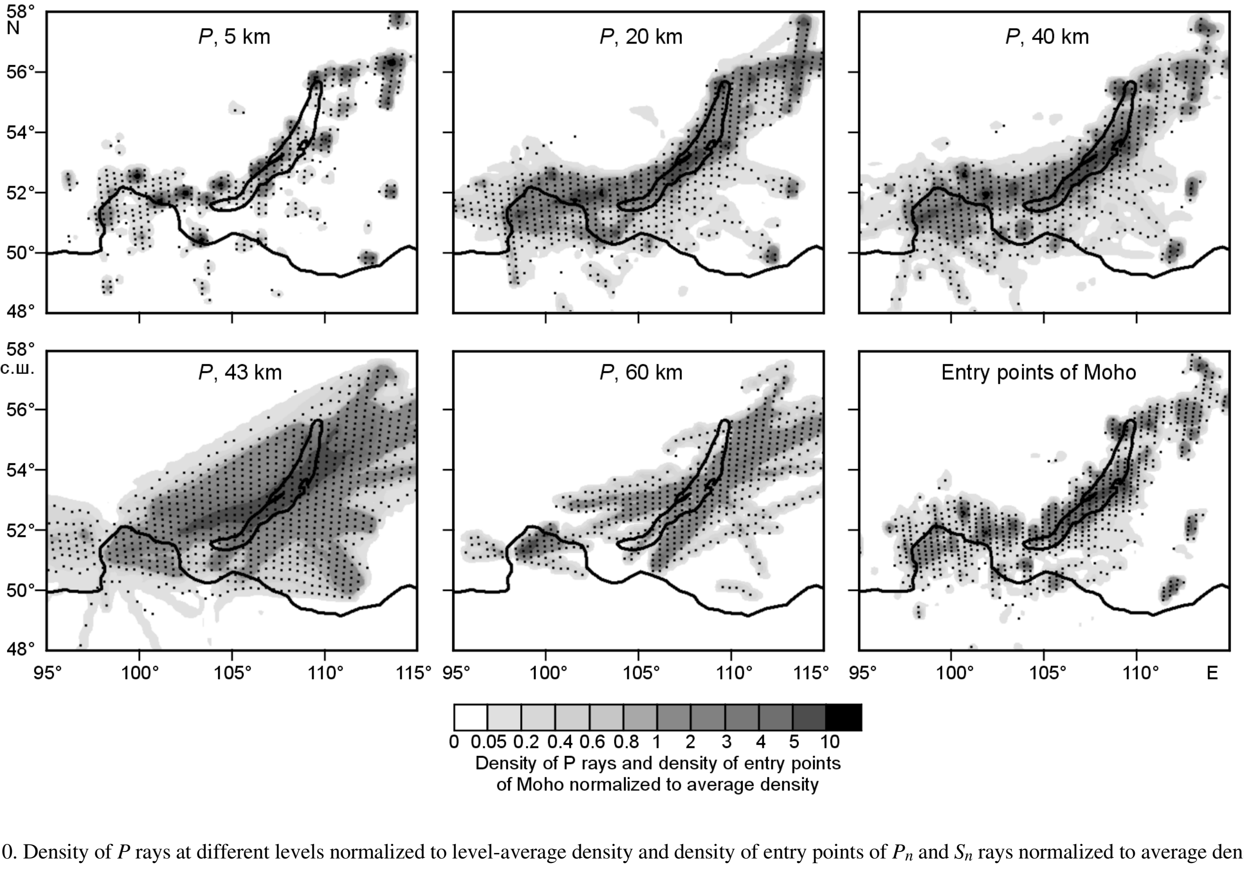

Fig. 10. Density of P rays at different levels normalized to level-average density and density of entry points of P_n and S_n rays normalized to average density.

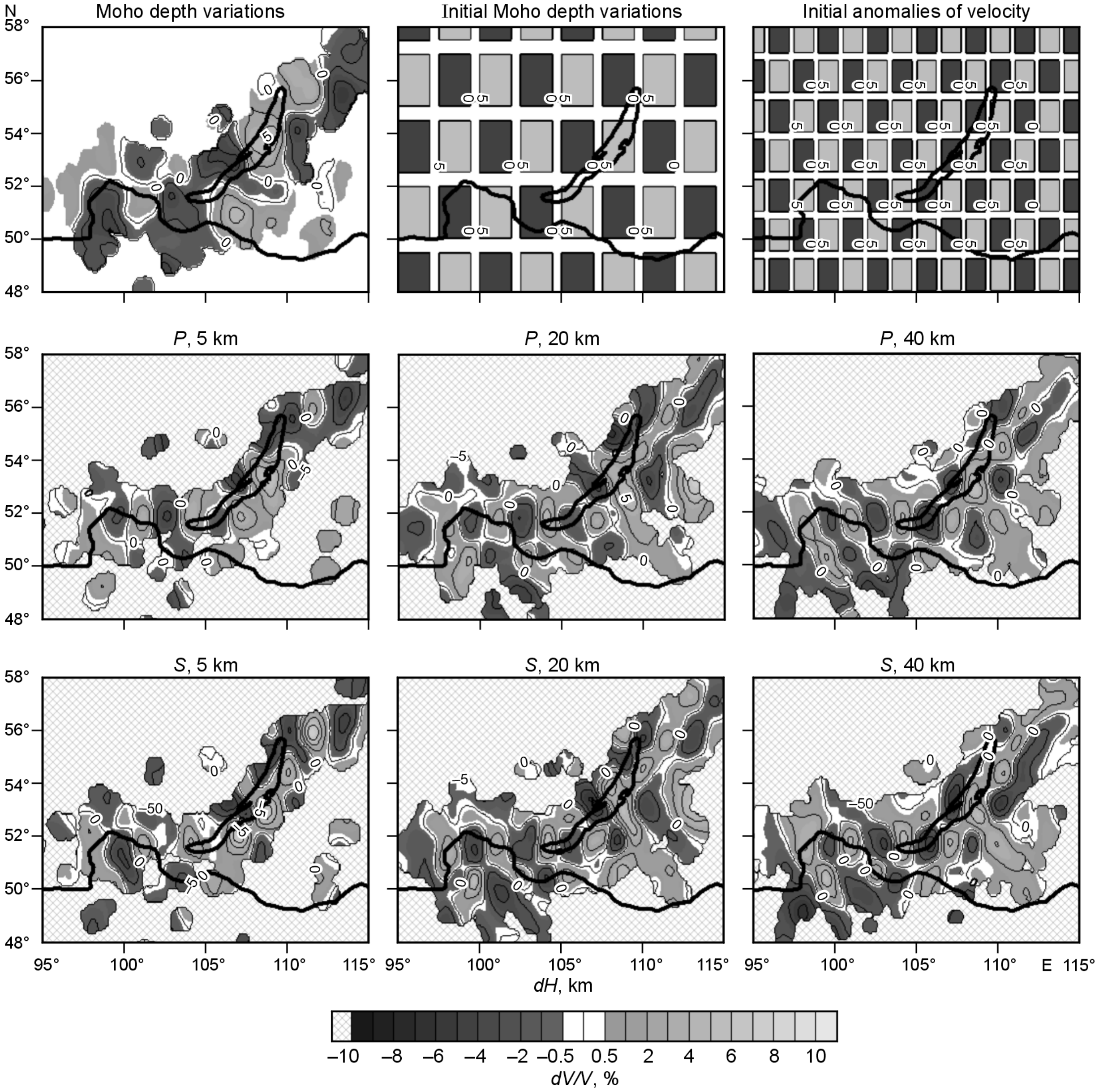

Fig. 11. Chequerboard test. Initial Moho depth and velocity patterns and inversion results at different depths with preliminary source location.

the layer from 0 to 50 km. The input arrivals used in inversion were obtained by adding a random number to synthetic travel times from each source. Then we applied the complete inversion procedure for source locations and origin times with the above algorithms (Fig. 11). In Table 2 the results are correlated to the initial distribution of anomalies. The test demonstrates the resolving power of the suggested algorithm and highlights the problem of diffused anomaly contours inherent to seismic tomography whereby the imaged anomalies are of lower intensity and occupy larger areas.

Test for the effect of shallow velocity anomalies on deeper structure. This test shows the effect of a prominent anomaly in the upper section on velocity anomalies in the lower section and on Moho depths. We used a 5% negative synthetic anomaly at depths between 0 and 15 km and computed travel times in the same way as in the previous test (Fig. 12). The presence of a shallow velocity anomaly causes almost no influence on Moho depth variations and the deep velocity structure.

Test with odd and even sources. To estimate the effect of random noise on the final result we inverted the data arbitrarily divided into two equal groups where earthquakes were assigned odd and even numbers. The results of inversion separately for even and odd sources (Figs. 13 and 14) indicate that noise causes different effects on the velocity and Moho depth patterns. The most reliable images are for P velocity anomalies. The results for S waves include a number of noncorrelated anomalies which are evident noise artefacts. Moho depth variations (Fig. 14) obtained from independent data sets likewise have some differences, i.e., the result is

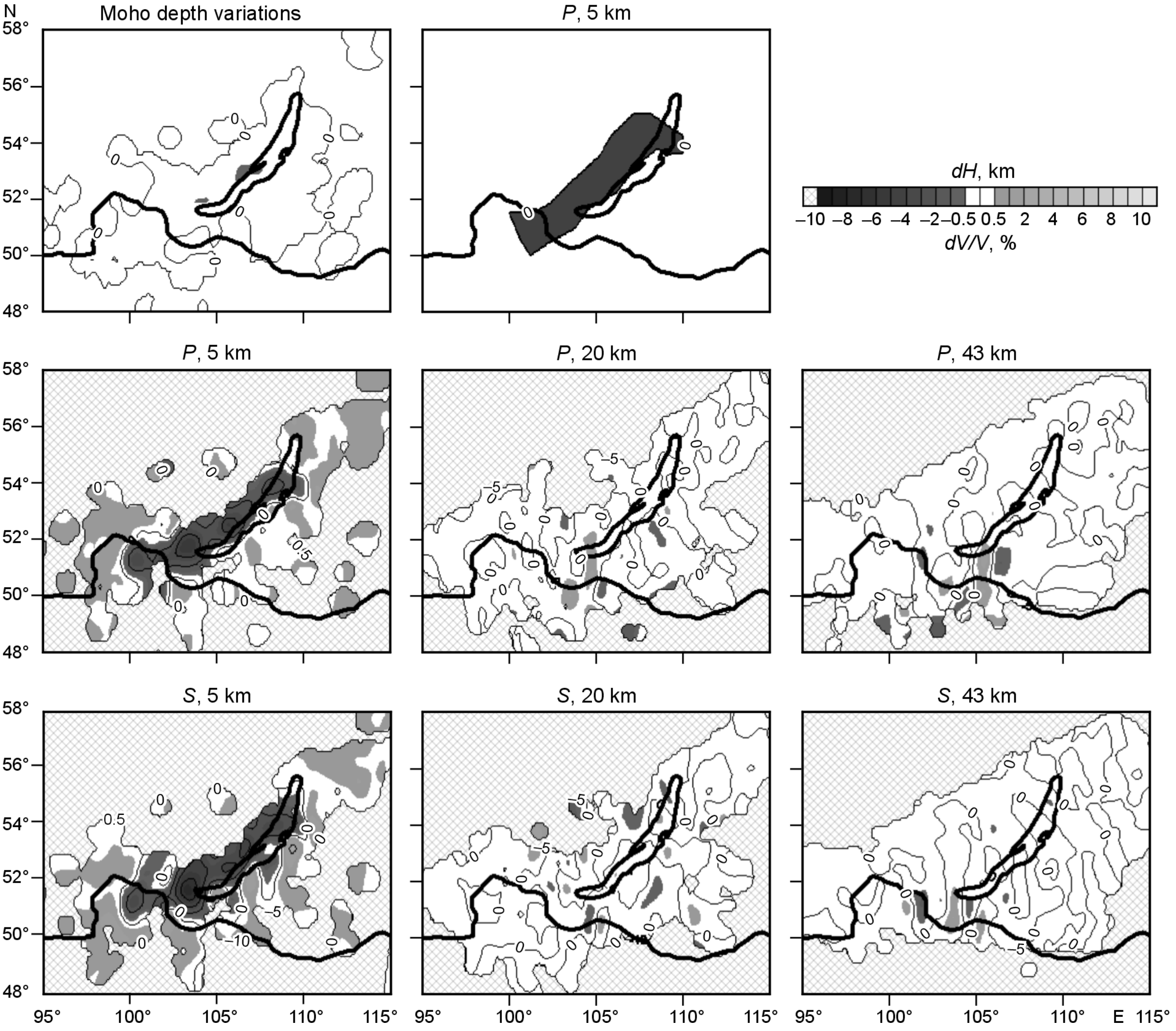

Fig. 12. Test for effect of a shallow anomaly on deeper structure. Inversion results.

highly sensitive to random noise. The models are correlated in Table 3. This test appears to be the best check for reliably inverted anomalies.

Inversion results for real data. *Source location.* Figure 15 shows the inversion results for final source location in the Baikal region. The greatest part of the earthquakes fall into the rift basins of highest seismicity (Busiyngol, South Baikal, and Muya) and cluster along large faults. Most events originate at depths from 0 to 10 and from 15 to 25 km (see the depth histogram of hypocenters after inversion in Fig. 16). Shallow earthquakes tend to the rift flanks and earthquakes within the central segment of the rift system have deeper hypocenters (Fig. 15). Almost all hypocenters are within the crust. Those below the Moho are obtained for far-field regions where source location bears the greatest error. The depths of hypocenters in our model agree with published data (e.g., Radziminovich et al., 2003).

Velocity anomalies: results and discussion. Inversion results for *P* and *S* velocity anomalies at different depths in the crust and upper mantle are given in Fig. 17. The images are the weighted sum of data from four parameterization grids of different orientations. Velocity values are mapped if their distances from the next node are below 40 km. The resolution appears rather high as the nodes correspond to sites of high ray density (Fig. 10). Resolution can be also checked in synthetic tests (Figs. 11, 12) and the reliability of anomalies in the test with odd-even sources (Figs. 13, 14).

The velocity pattern of crust and upper mantle images major regional structures. Note that our images show no prominent anomalies which would contour the Baikal rift as in many earlier studies, neither in the crust nor in the mantle (Fig. 1). Specifically, the velocity pattern beneath the Baikal basin is much more ambiguous than that reported in (Puzyrev, 1981; Rogozhina and Kozhevnikov, 1979).

The regional center of activity in our maps falls into the southwestern Baikal rift system where a low-velocity zone is clearly traceable at all depths in both *P* and *S* models. The anomaly underlies several basins (Busiyngol, Darhat, Hovsgol, and Tunka) of presumably rift origin (Fig. 1), and its geometry matches the field of Cenozoic volcanism (Fig. 1). Therefore,

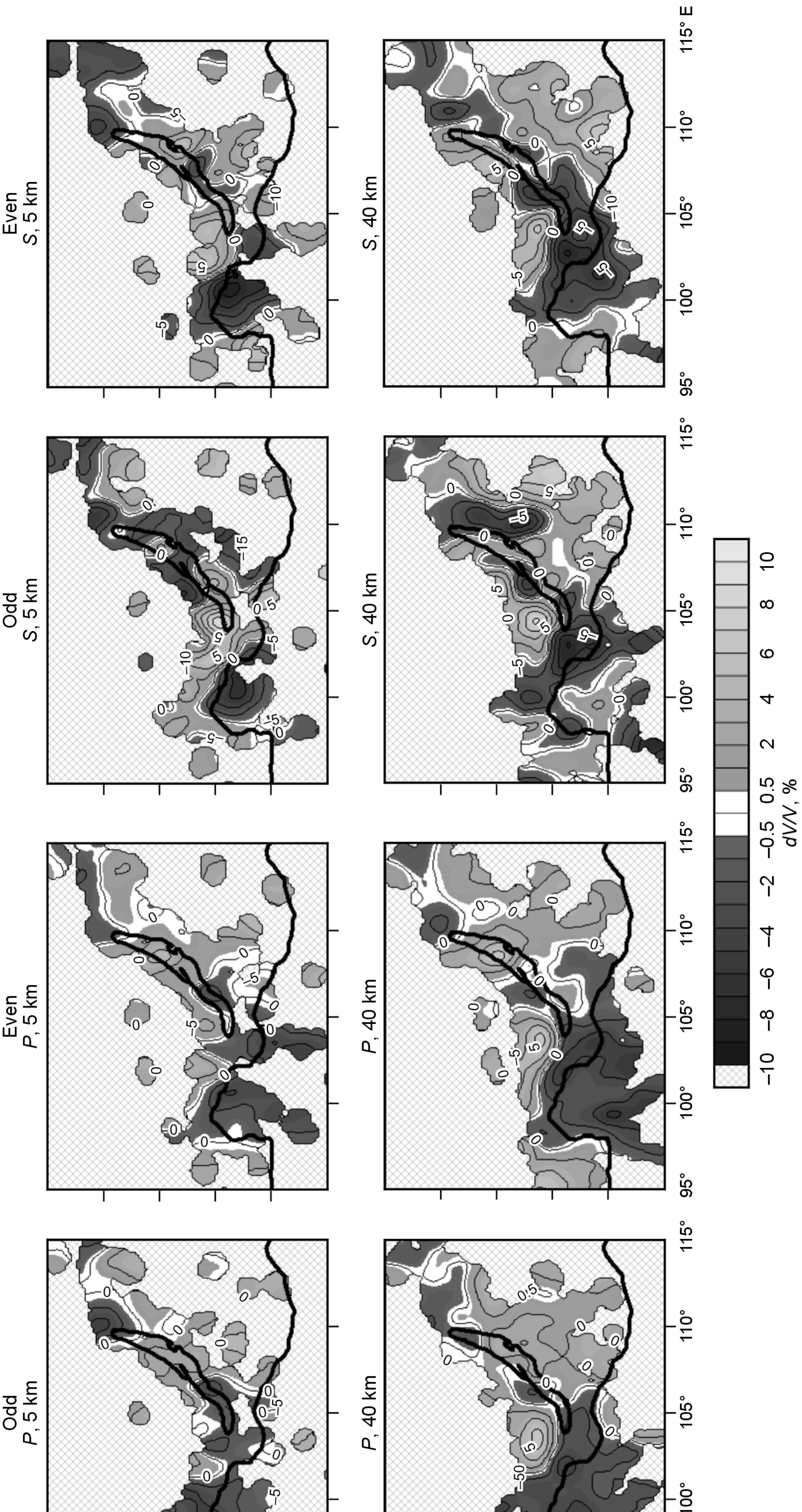

Fig. 13. Results of velocity inversions from two independent data sets (odd and even sources).

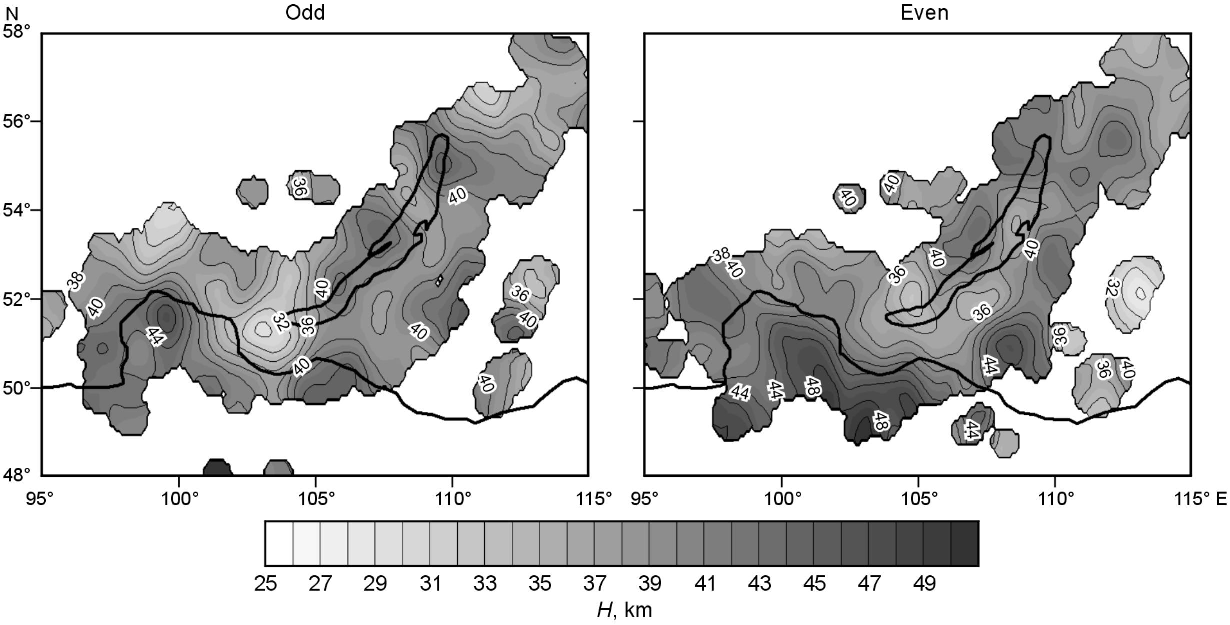

Fig. 14. Moho depths, from inversion of two independent data sets (odd and even sources).

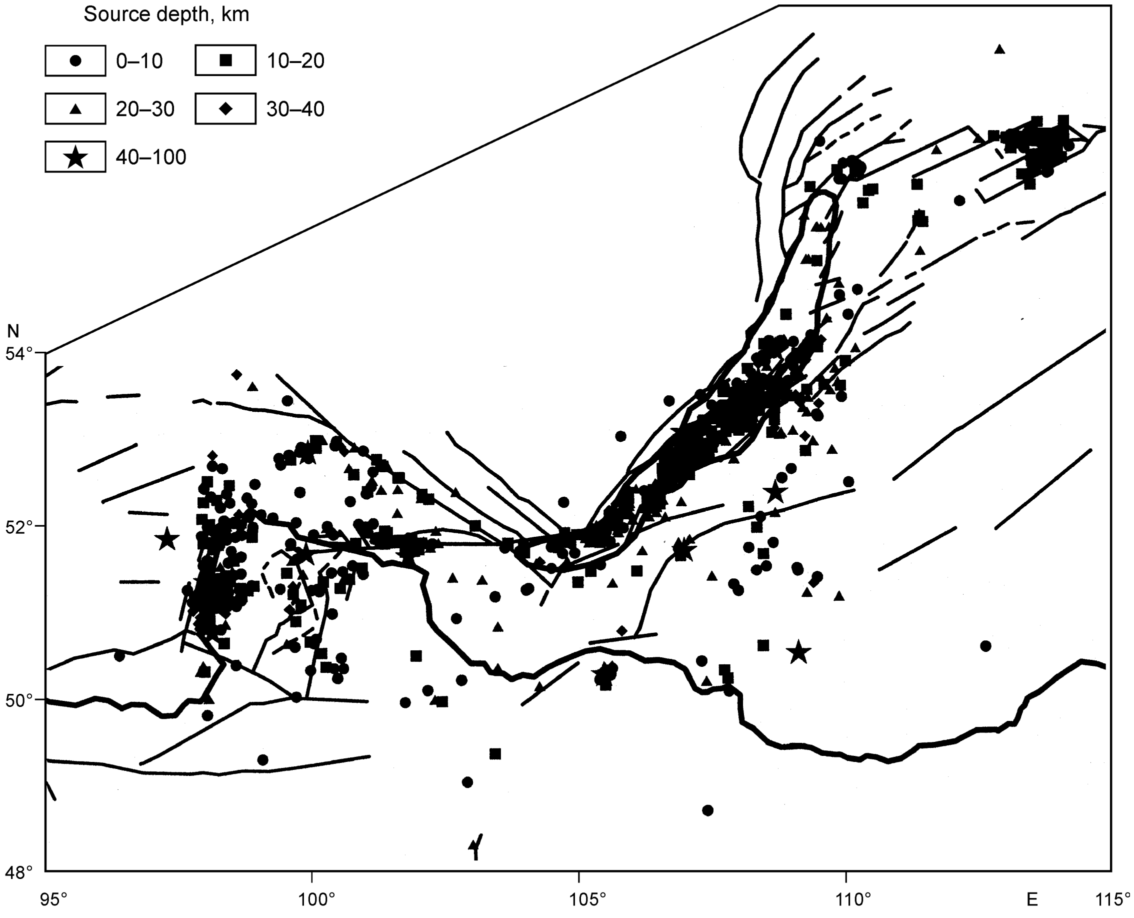

Fig. 15. Locations of epicenters after inversion.

the low velocities may be due to heating of the crust and the underlying mantle which might support the idea that rifting was induced by heating from a mantle plume and the ensuing weakening and extension of the lithosphere. Yet, this idea is inconsistent with the heat flow field beneath the rift (Fig. 3), not very prominent against the surrounding higher-velocity

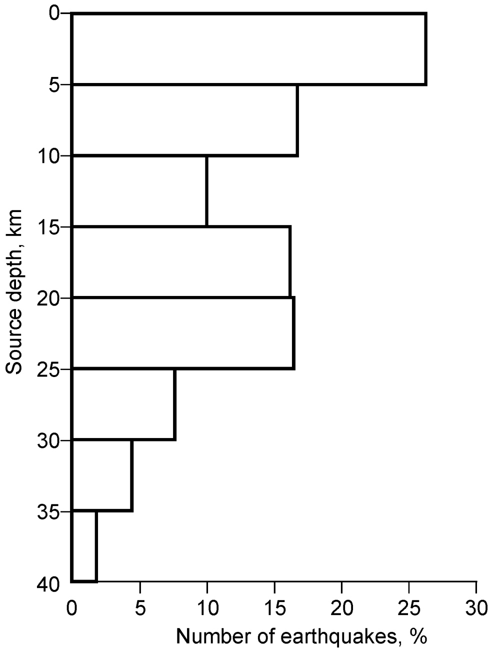

Fig. 16. Locations of hypocenters after inversion.

regions. Heat flux is slightly higher beneath the rift but the contrast is much weaker than one would expect in the case of total lithospheric heating. Furthermore, rifting is the most intense beneath Lake Baikal where the velocity pattern is quite ambiguous. If lithospheric heating were the leading process, extension would be the most rapid southwest of Lake Baikal in the area of volcanism.

Thus, volcanism in the low-velocity area is rather a consequence of lithospheric extension. The rise of mantle material due to lithospheric thinning apparently decreased the melting temperature as a result of decompression. Therefore, partial melting and volcanism were possible without strong lithospheric heating.

The origin of crustal and upper mantle low-velocity zones beneath the Baikal rift remains open to discussion. The anomaly can hardly be attributed to rock compositions in view of the great size of the low-velocity area and the complex regional geology. On the other hand, the heat flow evidence is against its origin by heating, at least as a leading process. Low velocities are most likely due to fluids and melts produced by mantle decompression. Furthermore, wave propagation in zones of active deformation, such as the Baikal rift, can be slowed down by small and large faults and fractures. This structural effect is especially well pronounced against the stable Siberian craton where seismic velocities are relatively high. The Main Sayan Fault, which separates the Siberian plate from its folded southern periphery, perfectly fits the boundary between the low- and high-velocity zones.

The subsurface beneath Lake Baikal and its nearest surroundings shows a quite heterogeneous velocity pattern. *P* and *S* anomalies have almost no correlation at a depth of 5 km, possibly, because of composition effects which can be essential in the shallow crust, but correlate well at greater depths. The match of even small anomalies, detected at the resolution limit, may be evidence of a rather high reliability of the images, though there is no good agreement between the surface and subsurface orientations of major tectonic elements. Large mountains and valleys in the immediate vicinity of Baikal strike along the lake while the velocity anomalies show up as alternating spots oriented across it. They apparently record the structure of crustal blocks welded into the craton edge in the prerift history of the region. Note that the northern half of Lake Baikal is paradoxically marked by a high-velocity zone in the crust and in the subcrustal mantle. This fact counts in favor of passive rifting in which the rifted lithosphere is never subject to total heating.

Low-velocity zones in the crust northeast of Lake Baikal fit the Upper Muya, Muya, Upper Angara, and Tsypa rift basins but the anomalies are weaker than in the southwestern flank of the rift system.

Moho depth: results and discussion. Inversion results for crust thickness in the model assuming a flat Moho at 40 km (Fig. 18,) were obtained after four iterations of simultaneous inversion of *P* and *S* velocity fields, source location, and station corrections. The crust thickness is estimated as an average over inversions with four different orientations of the parameterization grid. The Moho depths are mapped if their distances from the next node are within 40 km.

The final Moho depth map for the starting model (Bassin, 2000) of a variable crust thickness (Fig. 18, *b*) retains the general features of the latter (Fig. 2, *c*): the crust is thin beneath southern Baikal and thick beneath the East Sayan and Hentiyn mountains. At the same time, the crust beneath Baikal is thinner than in the starting model (30–31 km against 36–37 km) and two more lows of 40 and 36 km appear beneath central and northern Baikal, respectively. The results for invariable and variable Moho depths show a good agreement, i.e., the suggested inversion algorithm for the Moho depth is stable and quite independent of the starting model.

We chose the model obtained with the flat-Moho starting model as our final result. We cannot decide between the too controversial available models for the Baikal region to take for reference in our study.

The inverted Moho depths depart quite considerably from 40 km assumed in the starting model. The crust is as thin as 32 km at the southern tip of Lake Baikal and 36 km at the southeastern edge of the Siberian craton. A thin crust of 34 km occurs beneath the Sangilen block in the Tuva-Mongolia microcontinent (50–51° N, 98–99° E). The greatest crust thickness reaches 46–47 km between 49 and 51° N and 101 and 104° E. However, the Moho in the East Sayan region is slightly shallower than expected according to Zorin's (Logatchev and Zorin, 1987) and Suvorov's (Suvorov et al., 2002) models (40–43 km against 45–50 km).

The Moho depths match quite well the major surface structures, with thicker crust beneath rift ridges (42–46 km in North Mongolia at 49–50° N, 100–104° E) and thinner crust beneath rift basins (30 and 34 km under the Tunka and Busiyngol basins, respectively). The same consistency is observed around the Baikal basin: areas of greatest extension

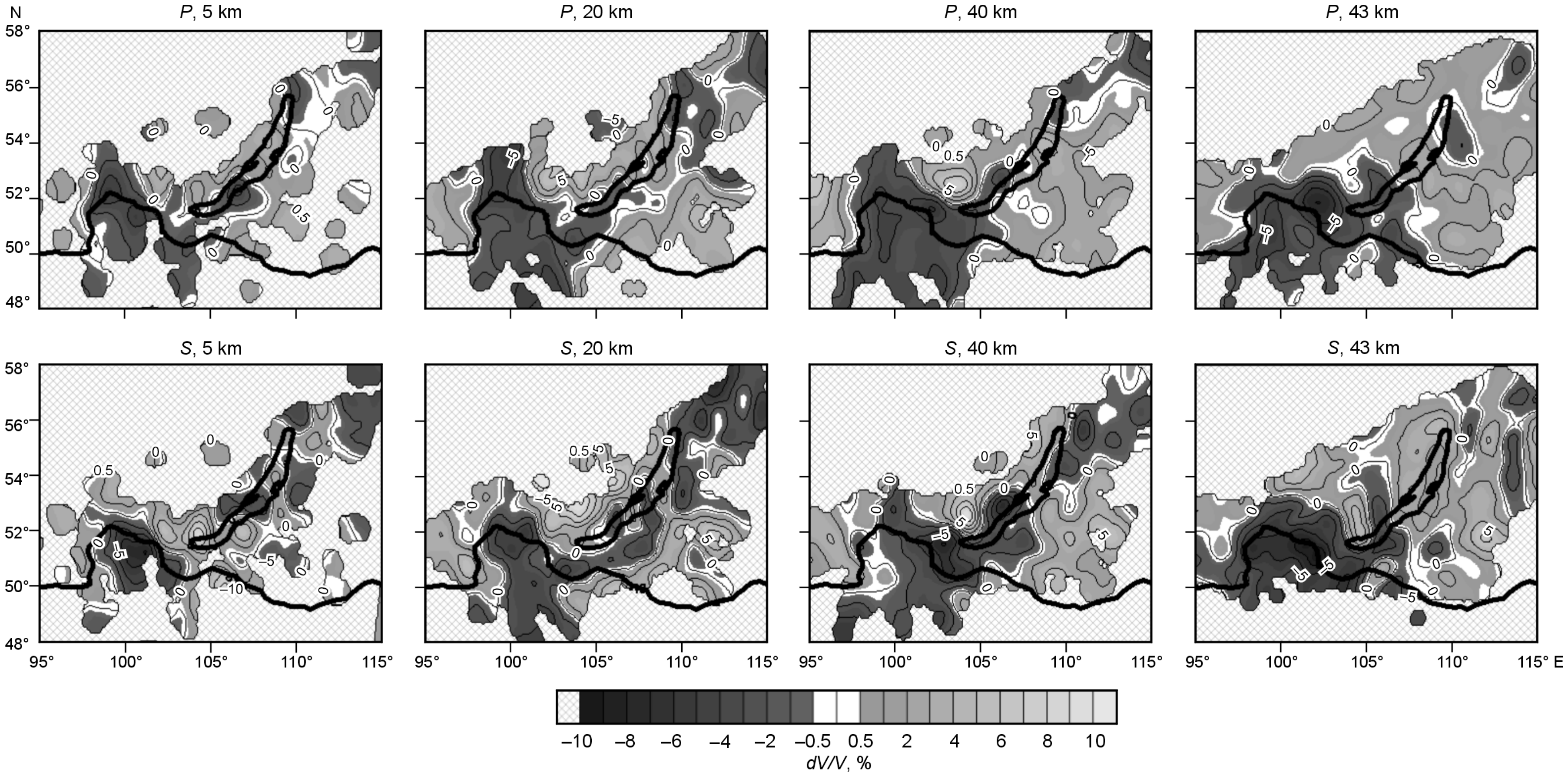

Fig. 17. *P* and *S* velocity anomalies at different crustal depths. Main inversion result.

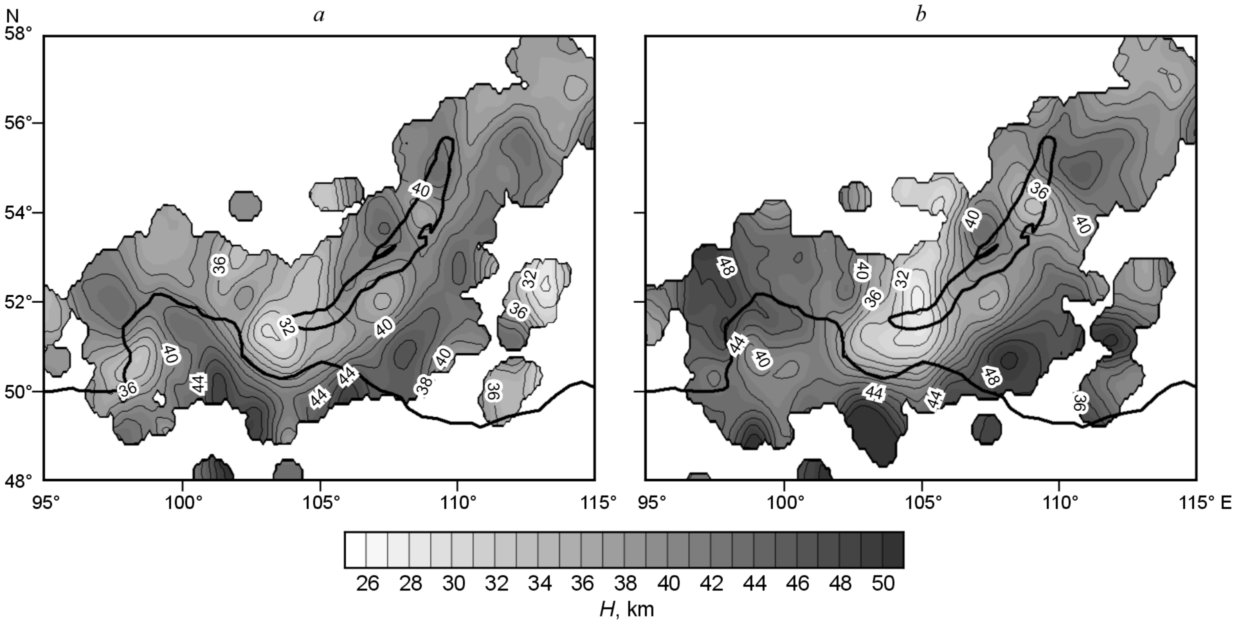

Fig. 18. Crust thickness. Main inversion result. *a* — uniform starting model, with flat Moho at 40 km; *b* — starting model with 2°×2° resolution (Radziminovich et al., 2003).

along the lake and in its southeastern part are marked by an elongate zone of thin crust. Mountains in Transbaikalia and the Primorsky Ridge on the Siberian craton margin fall into the area of thick crust. Rift basins in the northeastern rift flank are underlain by a slightly attenuated crust of 37 km. Therefore, the Moho topography in the Baikal rift system appears to be generally controlled by crustal extension and compression.

The basic difference between the velocity and Moho depth patterns indicates the ability of tomography to discriminate between the two parameters.

Our inversion results for Moho depths (Fig. 2) are generally in line with the published models (Logatchev and Zorin, 1987; Suvorov et al., 2002) that suggest thicker crust beneath the East Sayan and Hentiyn mountains and thinner crust near Irkutsk; the position of three local lows beneath Lake Baikal agrees with the results by Zorin (Logatchev and Zorin, 1987). Discrepancies in details may be due to difference in the used geophysical methods.

Conclusions

The reported velocity (Fig. 17) and Moho depth (Fig. 18) images allow the following inferences:

— The upper mantle velocity structure (Fig. 17) shows no large low-velocity zone beneath the whole Baikal rift system predicted in (Puzyrev, 1981; Rogozhina and Kozhevnikov, 1979).

— The most prominent velocity low in the crust and upper mantle is located in the southwestern flank of the Baikal rift system and coincides with the area of Cenozoic volcanism. Wave propagation in this area may be slowed down by fluids and melts produced by mantle decompression. The crustal velocity lows can result from small and large faults and fractures in this region of active deformation.

— The Siberian plate shows up as a high-velocity zone. Its contrast with the low-velocity southwestern Baikal rift suggests that homogeneity of rocks causes the key effect on crustal velocities.

— Velocity anomalies in the central Baikal rift mismatch the geometry of surface structures. They may mark the position of blocks accreted to Siberia during the prerift history.

— The Moho depth map images a thin crust along Lake Baikal which is consistent with the general concept of rifting. Moho depths have a generally better fit to the surface tectonics than the crustal velocities.

The suggested source location algorithm is especially useful for low-quality data. It can provide a check for earlier paper databases from analog data acquisition. The relocated sources give a more faithful image of the Earth's deep structure on both global and regional scales.

The reported evidence of the crustal structure has different geological and geophysical applications and can be used for reference in numerical modeling of geodynamic processes in the Baikal rift. The new velocity and Moho depth models are applicable to updating earthquake source parameters in the Baikal region. Another use of the Moho depth model is for subtracting the effect from crustal structures and Moho depth variations to better highlight the mantle in gravity modeling. Furthermore, it can help gaining a more faithful image of the upper mantle in teleseismic tomography.

The reported models can be further updated. First, we expect to use new catalog data missed in this study. Second, we plan to address the anisotropy problem. According to recent reports (Rompker et al., 2003, etc.), travel time difference between fast and slow directions can reach a few seconds in some regions (e.g., vicinity of the San Andreas Fault in California or the Dead Sea in Asia Minor), which strongly exceeds the contribution of isotropic seismic anomalies. The expected anisotropy in the Baikal region is not as high as that but its influence can be quite large. Therefore, further updating the algorithm will aim at obtaining an anisotropic velocity model applicable to the Baikal data.

References

Achauer, U., Masson F., 2002. Seismic tomography of continental rifts revisited: from relative to absolute heterogeneities. Tectonophysics 358, 17–37.

Bassin, C., Laske, G., Masters, G., 2000. The current limits of resolution for surface wave tomography in North America. EOS Trans AGU 81, F897.

Belousov, V.V., Pavlenkova, N.I., Egorkin, A.V., 1991. Deep structure of the USSR territory (in Russian). Nauka, Moscow.

Bijwaard, H., Spakman, W., Engdahl, E., 1998. Closing the gap between regional and global travel time tomography. J. Geophys. Res. 103 (B12), 30055–30078.

Burov, E.B., Houdry, F., Diament, M., Deverchere, J., 1994. A broken plate beneath the North Baikal rift zone revealed by gravity modeling. Geophys. Res. Lett. 21 (2), 129–132.

Calais, E., Vergnolle, M., San'kov, V., Lukhnev, A., Miroshnitchenko, A., Amarjargal, S., Deverchere, J., 2003. GPS measurements of crustal deformation in the Baikal-Mongolia area, 1994–2002. J. Geophys. Res. 108 (B10).

Chemenda, A., Deverchere, J., Calais, E., 2002. Three-dimensional laboratory modeling of rifting: Application to the Baikal Rift, Russia. Tectonophysics. 356, 253–273.

Deverchere, J., Petit, C, Gileva, N., Radziminovitch, N., Melnikova, V., San'kov, V., 2001. Depth distribution of earthquakes in the Baikal rift system and its implications for the rheology of the lithosphere. Geophys. J. Int. 146(3), 714–730.

Dorofeeva, R.P., Sintsov, A.A., 1990. Heat flow of southeastern Transbaikal and eastern Mongolia. Geologiya i Geofizika (Soviet Geology and Geophysics). 31 (9), 130-141(123-133).

Duchkov, A.D., Lysak, S.V., Balobaev, V.T. (Eds.), 1987. The geothermal field of Siberia (in Russian). Nauka, Novosibirsk.

Duchkov, A.D., Sokolova, L.S., 1974. Geothermal studies in Siberia (in Russian).Nauka, Novosibirsk.

Khain, V.E., 2001. Tectonics of oceans and continents (in Russian). Nauchnyi Mir, Moscow.

Koulakov, I., Tychkov, S., Bushenkova, N., Vasilevskiy, A., 2002. Structure and dynamics of the upper mantle beneath the Alpine-Himalayan orogenic belt, from teleseismic tomography. Tectonophysics 358, 77–96.

Krylov, SV., Golenetskii, SI., Petrik, G.V., 1974. Correlation of seismology and DSS data on the structure of upper mantle in the Baikal rift zone. Geologiya i Geofizika (Soviet Geology and Geophysics) 15(12), 61–66.

Kulakov, I.Yu., 1999. Three-dimensional seismic inhomogeneities beneath the Baikal region according to teleseismic and local tomography. Geologiya i Geofizika (Russian Geology and Geophysics) 40 (3), 317–331(317-330).

Lesne, O., Calais, E., Deverchere, J., Hassani, R., Chery, J., 2000. Dynamics of intracontinental extension in the North Baikal Rift from two-dimensional numerical deformation modeling. J. Geophys. Res. 105, 21727–21744.

Logatchev, N.A, Zorin, Y.A., 1987. Evidence and causes of the two-stage development of the Baikal rift. Tectonophysics 143, 225–234.

Logatchev, N.A., 1993. History and geodynamics of the lake Baikal rift in the context of the Eastern Siberia rift system: a review. Bull. Centres Rech. Explor. — Prod. Elf Aquitaine 17 (2), 353–370.

Lysak, S.V., 1984. Terrestrial heat flow in the south of East Siberia. Tectonophysics 103, 205–215.

Lysak, S.V., 1988. Heat flow of continental rift zones (in Russian). Nauka, Novosibirsk.

Mordvinova, V.V., Vinnik, L.P., Kosarev, G.L., Oreshin, S.I., Treusov, A.V., 2000. Teleseismic tomography of the Baikal rift lithosphere. Dokl. Earth Sci. 372 (4), 716.

Nicolas, A., Achauer, U., Daignieres, M., 1994. Rift initiation by lithospheric rupture. Earth Planet. Sci. Lett. 123, 281–298.

Paige, C.C., Saunders, M.A., 1982. LSQR: An algorithm for sparse linear equations and sparse least squares. ACM Trans. Math. Soft. 8, 43–71.

Peltzer, G., Tapponnier, P., 1988. Formation and evolution of strike-slip faults, rifts and basins during the India-Asia collision: An experimental approach. J. Geophys. Res. 93, 15095–15117.

Petit, C., Koulakov, I., Deverchere, J., 1998. Velocity structure around the Baikal rift zone from teleseismic and local earthquake traveltimes and geodynamics implications. Tectonophysics 296, 125–144.

Puzyrev, N.N. (ed.), 1981. Interior of Baikal, from seismic data (in Russian). Nauka, Novosibirsk.

Puzyrev, N.N. (ed.), 1993. Detailed P- and S-wave seismic studies (in Russian). Nauka, Novosibirsk.

Radziminovich, N.A., Balyshev, C.O., Golubev, V.A., 2003. Earthquake focal depths and crustal strength in the Baikal rift. Geologiya i Geofizika (Russian Geology and Geophysics) 44 (11), 1216–1225(1175-1183).

Radziminovitch, N.A., Deverchere, J., Melnikova, V., San'kov, V.A., Giljova, N., 2005. The 1999 Mw 6.0 earthquake sequence in the Southern Baikal rift, Asia, and its seismotectonic implications. Geophys. J. Int. 161, 387-400.

Rogozhina, V.A., Kozhevnikov, V.M., 1979. An anomalous mantle zone beneath the Baikal rift (in Russian). Nauka, Novosibirsk.

Rumpker, G., Ryberg, T., Vosk, G. & Desert Seismology Group, 2003. Evidence for boundary-layer mantle flow beneath the Dead Sea Transform from seismic anisotropy. Nature 425, 497–501.

Suvorov, V.D., Mishenkina, Z.M., Petrick, G.V., 2002. Structure of the crust in the Baikal rift zone and adjacent areas from Deep Seismic Sounding data. Tectonophysics 351, 61–74.

Tiberi, C., Diament, M., Deverchere, J., Petit-Mariani, C., Mikhailov, V., Tikhotsky, S., Achauer, U., 2003. Deep structure of the Baikal rift zone revealed by joint inversion of gravity and seismology. J. Geophys. Res. 108 (B3), 2133.

Van der Sluis, A., van der Vorst, H.A., 1987. Numerical solution of large, sparse linear algebraic systems arising from tomographic problems, in: Seismic tomography, Reidel, Dordrecht, pp. 49–83.

Waldhauser, F., Ellsworth, W.L., 2000. A double-difference earthquake location algorithm: method and application to the northern Hayward fault, California. Bull. Seis. Soc. Amer. 90 (6), 1353–1368

Youngsheng, Song, Krylov, S.V., Baojun, Yang, Cai, Liu, Shixue, Dong, Tiechen, Liang, Jingzhi, Li, Xingzui, Xu, Mishen'kina, Z.R., Petrik, G.V., Shelud'ko, I.F., Seleznev, V.S., Sokolov, V.M., 1996. Deep seismic sounding of the lithosphere on the Baikal — Northeastern China International Transect. Geologiya i Geofizika (Russian Geology and Geophysics) 37 (2), 3–15(1–13).

Zonenshain, L.P., Savostin, L.A., 1980. Geodynamics of the Baikal rift zone and plate tectonics of Asia. Tectonophysics 76, 1–45.

Zorin, Y.A., Mordvinova, V.V., Turutanov, E.Kh., Artemiev, A.A., Kosarev, G.L., Gao, S.S., 2002. Low seismic velocity layers in the Earth's crust beneath Eastern Siberia (Russia) and Central Mongolia: receiver function data and their possible geological implication. Tectonophysics 359, 307–327.

Zorin, Y.A., Turutanov, E.Kh., Mordvinova, V.V., Kozhevnikov, V.M., Yanovskaya, T.B., Treussov, A.V., 2003. The Baikal rift zone: the effect of mantle plumes on older structure. Tectonophysics 271, 153–173.

Zorin, Yu.A., Turutanov, E.Kh., 2005. Plumes and geodynamics of the Baikal rift zone. Geologiya i Geofizika (Russian Geology and Geophysics). 46 (7), 685–699(669–682).